Comparing extracellular vesicles and cell membranes as biocompatible coatings for gold nanorods: Implications for targeted theranostics

Paula Maria Pincela Lins [a,*], Laís Ribovski [a], Luana Corsi Antonio [a], Wanessa Fernanda Altei [b,c], Heloisa Sobreiro Selistre-de-Araújo [b], Juliana Cancino-Bernardi [a], Valtencir Zucolotto [a,d]

[a] *Nanomedicine and Nanotoxicology Group, Physics Institute of São Carlos, University of São Paulo, São Carlos, SP, Brazil*
[b] *Laboratory of Biochemistry and Molecular Biology, Department of Physiological Sciences, Federal University of São Carlos, SP, Brazil*
[c] *Molecular Oncology Research Center, Barretos Cancer Hospital, SP, Brazil*
[d] *Institute of Advanced Studies, University of São Paulo, São Carlos, SP, Brazil*

ARTICLE INFO

ABSTRACT

Extracellular vesicles (EVs) and cell membrane nanoghosts are excellent coatings for nanomaterials, providing enhanced delivery in the target sites and evasion of the immune system. These cell-derived coatings allow the exploration of the delivery properties of the nanoparticles without stimulation of the immune system. Despite the advances reported on the use of EVs and cell-membrane coatings for nanomedicine applications, there are no standards to compare the benefits and main differences between these technologies. Here we investigated macrophage-derived EVs and cell membranes-coated gold nanorods and compared both systems in terms of target delivery in cancer and stromal cells. Our results reveal a higher tendency of EV-coated nanorods to interact with macrophages yet both EV and cell membrane-coated nanorods were internalized in the metastatic breast cancer cells. The main differences between these nanoparticles are related to the presence or absence of CD47 in the coating material, not usually addressed in EVs characterization. Our findings highlight important delivery differences exhibited by EVs- or cell membranes- coated nanorods which understanding may be important to the design and development of theragnostic nanomaterials using these coatings for target delivery.

1. Introduction

For almost a century, cancer was considered a monocellular disease [1,2]. However, recent studies have revisited the 'seed and soil' hypothesis which suggested that metastasis is favored when in a friendly organ microenvironment [2,3]. The concept of tumor microenvironment (TME), for example, including the interaction of cancer cells with the extracellular matrix (ECM), blood vessels, associated macrophages and fibroblasts, as well as the aspects concerning the circulating tumor cells, has been the focus of intense medical research aiming at elucidating tumor progression [4,5]. The complexity of the TME, in particular, may hinder conventional treatments using free chemotherapeutics, due to the low concentration of the active effectively delivered to the tumor site, which also results in severe side effects [6]. To overcome the latter effects, tumor vasculature has been explored as a means to accumulate nanoscale carriers and macromolecules in the target sites [7], a sized-related process known as *enhanced permeability and retention effect* (EPR) [8,9]. Despite the EPR effect, only 0.7% of the administered dose

of nanomedicines reaches the solid tumor [10,11].

When a nanomaterial is administered into the body, it encounters several obstacles imposed by our immune system [12,13], and therefore an efficient camouflage of the nanomaterials is important for a successful translation *in vivo* [14]. This is the case of tetraspanin CD47 which has a role in regulating phagocytosis from macrophages [15]. This protein is a ligand for the signal regulatory protein α (SIRPα) and has an inhibitory role in phagocytosis [16]. CD47 acts as a "self-marker" on some cells [17,18] being overexpressed in cancer cells [19–21]. Upon the interaction of CD47 and SIRPα, phagocytosis by macrophages is inhibited [17]. Evaluation of the CD47 expression and thus understanding the 'eat me/don't eat me' strategy is a paramount step for the smart delivery of chemotherapeutics using nanocarriers [22].

Biomimicking nanocarriers based upon cell membranes vesicles has been reported as efficient platforms for active delivery [23]. The cell-membrane coating technology was first reported in 2011 [24], and after 10 years, there is still room for improvement [25–27]. The main advantages of this technology comes from the fact that functionalized

* Corresponding author.
E-mail address: paula.lins@usp.br (P.M. Pincela Lins).

nanoparticles inherit important features from the source cells, including prolonged circulation time [24,28] and the ability to target tumor sites by homotypic binding [26,29–31].

Coatings based on extracellular vesicles (EVs) are also an important strategy to enhance circulation time [32,33], targeting [20,34,35] and modulation of tumor microenvironment [36,37]. EVs are known to interplay communication between cells depending on their donor cells and origin [33]. These membrane-bound carriers are classified by their size, as small (50–200 nm), medium (200–1000 nm), and large extracellular vesicles (1–10 μm) [38]. Small EVs originate from two forms by endosomal (exosomes) or plasma membranes (microvesicles) release (Fig. 1A) [39]. Although small EVs exhibit innate characteristics of long-distance communication, the current isolation methods and their yields are limited and pose several challenges for drug delivery and biomimetic coatings applications [40]. Thus, a validation regarding their functionality and a comparison with classical biomimetic nanoparticles could generate valuable information for their rapid translation into the clinics [33,41,42].

In this paper we compared the delivery properties of EVs- and membrane-coated nanorods, focusing on their ability to interact with cancer and stromal cells. Gold nanorods were chosen due to their use in photothermal therapy as theragnostic nanomaterials [23]. Our results shows the importance of CD47 molecules as the "do not eat me" signal in the cell membrane-derived nanoparticles. Additionally, cell membranes-coated NRs were able to interact the tumor cell lines more efficiently than the EVs-based gold nanorods, highlighting the importance of membrane composition during the development of nanomaterials for drug delivery.

2. Methodology

All reagents were used as purchased and the chemical solutions were prepared using ultrapure water (18.2 MΩ.cm at 25 °C). Glassware and magnetic bars were cleaned before each experiment using a fresh aqua
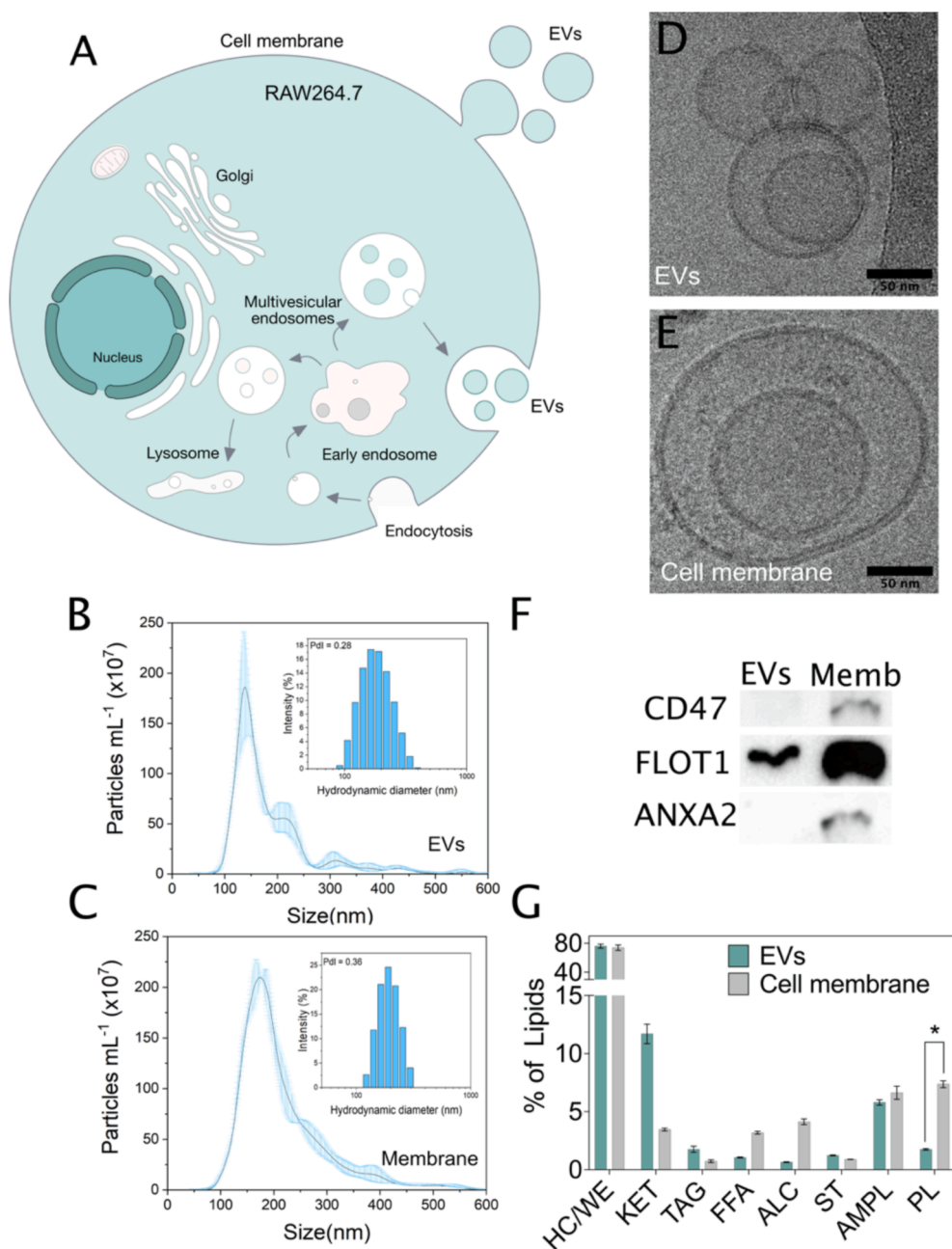
Fig. 1. Characterization of extracellular vesicles and membrane extract from RAW264.7 macrophages. (A) Schematic of the biogenesis of EVs. Size distribution of (B) extracellular vesicles and (C) cell membrane extract from RAW264.7 by NTA and DLS (insert). (D) EVs and (E) cell membrane extract microscopic analysis of their vesicular property after isolation by Cryo-TEM. Scale bar: 50 nm. (F) Western blot analysis using anti-CD47, anti-Flotilin 1(FLOT1), and anti-Annexin 2 (ANXA2). G) Lipid composition analysis as revealed by Iatroscan.

regia solution (HCl and HNO$_3$ in 1:3 ratio). The reagents used in cell cultures were previously autoclaved and the procedures performed in a laminar flow chamber using sterile materials.

2.1. Synthesis of the gold nanorods

The synthesis of gold nanorods was based on seed-mediated growth in the presence of the surfactant cetyltrimethylammonium bromide (CTAB, Sigma Aldrich) [43]. The gold seeds suspension was prepared by mixing 9.75 mL of 0.1 mol L^{-1} CTAB with 250 µL of 0.01 mol L^{-1} HAuCl$_4$ (Sigma Aldrich) and left under stirring for one minute. Then, 600 µL of cold 0.01 mol L^{-1} NaBH$_4$ (Sigma Aldrich) was added to the solution and left under stirring for 10 min. This suspension was maintained at 25 °C for 1.5 h before use.

Following, 2 mL of 0.01 mol L^{-1} HAuCl$_4$ were mixed with 36 mL of 0.1 mol L^{-1} CTAB. To this mixture, 120 µL of 0.01 mol L^{-1} AgNO$_3$ (Sigma Aldrich), 800 µL of 1 mol L^{-1} HCl (Synth), and 320 µL of 0.1 mol L^{-1} ascorbic acid (Sigma Aldrich) were added sequentially. Finally, 4 mL of the previously prepared gold seeds were added. The system was maintained at room temperature for at least 24 h and then centrifuged (5 times) at 1500×g for 5 min to remove CTAB excess.

Removal of CTAB (which is highly cytotoxic [44]) and the further functionalization of the NRs with citrate were carried out as follows: 20 mL of CTAB_AuNR were centrifuged three times (16,000×g, 85 min). Next, the AuNR pellet was redispersed in 0.15 wt% poly(sodium 4-styrene sulfonate (Na-PSS, molecular weight of 70,000) to a final volume of 20 mL and left to stand for at least 2 h before the next step. This sample was submitted to two centrifugation steps (16,000×g, 85 min) and redispersed in 0.15 wt% of Na-PSS to a final volume of 10 mL. The latter step is needed to ensure efficient removal of CTAB. Finally, the samples were centrifuged and redispersed in 20 mL of sodium citrate (Sigma Aldrich) at 5 mmol L^{-1}, keeping at rest for at least 12 h. The dispersion was subjected to the second cycle of centrifugation, with a final volume of 5 mL dispersed in sodium citrate 5 mmol L^{-1}. For functionalization studies, the NRs were submitted to a third cycle of centrifugation and resuspended in phosphate buffered saline (PBS) 1×.

The AuNR_PEG nanomaterials employed in the cell viability studies were produced as following: After removing the excess of CTAB, PEG-SH (Sigma Aldrich) was added to the gold nanorods dispersion to a final concentration of 200 µmol L^{-1} and sonicated for 30 min. The nanoparticles were gently shaken overnight at room temperature and then centrifuged to remove the excess of free polymer.

2.2. Cell culture

Macrophage Abelson murine leukemia virus-transformed (RAW264.7, American Type Culture Collection, ATCC), healthy fibroblasts (L929, ATCC), rat hepatoma (HTC, BCRJ), and healthy mouse liver (FC3H, BCRJ) cells were cultured in Dulbecco's Modified Eagle Medium (DMEM, Vitrocell, Brazil) supplemented with 10% (v/v) of fetal bovine serum (FBS, Vitrocell, Brazil), and 1% (v/v) L-Glutamine at 37 °C in a humidified atmosphere with 5% CO$_2$. Metastatic breast cancer cells (4T1) were acquired from the Rio de Janeiro Bank Cell (BCRJ) and cultured in Roswell Park Memorial Institute Medium (RPMI, Vitrocell, Brazil) supplemented with 10% (v/v) of fetal bovine serum (FBS, Vitrocell, Brazil) at 37 °C in a humidified atmosphere with 5% CO$_2$.

2.3. Extracellular vesicles isolation

RAW264.7 cells were cultured in 175 cm^2 flasks (Greiner). After 70% of confluence, the culture media was replaced by DMEM supplemented with 1% (v/v) L-Glutamine and 10% (v/v) FBS depleted of exosomes (Thermo Fisher Scientific). Cell culture medium was collected at 24 or 48 h, depending on the confluency, and centrifuged at 800×g for 4 min at room temperature to remove detached cells. To avoid contamination by larger vesicles, such as apoptotic bodies, the supernatant was

submitted to filtration with a membrane with a pore size of 0.22 µm [45]. Filtered supernatant was ultracentrifuged at 100,000×g for 2 h at 4 °C. The pellet was washed with (PBS) followed by a second ultracentrifugation step at 100,000×g for 2 h at 4 °C using an Optima MAX-XP ultracentrifuge (Beckman Coulter, TLA 110 rotor). The pellet was collected and resuspended in PBS containing SIGMAFAST^{TM} protease inhibitor cocktail tablets prepared according to manufacturer specifications. For long-term storage, the EVs were stored at −80 °C and used within 1 month after isolation. EVs were characterized in size distribution and concentration by dynamic light scattering (DLS, Zetasizer Nano ZS, Malvern), Cryo-TEM, and nanoparticle tracking analysis (NTA, Nanosight NS300, Malvern). We have submitted all relevant data of our experiments to the EV-TRACK knowledgebase (EV-TRACK ID: EV210114) [46].

2.4. Cell membrane extraction

RAW264.7 cells in 70% confluence (175 cm^2 flasks) were detached from the flask using a cell scraper and subsequently centrifuged at 800×g for 5 min at room temperature. The pellet was centrifuged (800×g, 5 min) and washed at least two times with PBS. The pellet was then resuspended with hypotonic buffer (10 mM Tris base, 1.5 mM MgCl$_2$, 10 mM NaCl, pH 6.8, all Sigma Aldrich), and after 5 min, sedimentation was performed by centrifugation at 800×g, for 5 min, at 4 °C. The pellet was resuspended in lysis buffer (0.25 M sucrose, 10 mM HEPES, 100 mM succinic acid, 1 mM EDTA, 2 mM CaCl$_2$, 2 mM MgCl$_2$, pH 7.4, all Sigma Aldrich), and the final solution was homogenized 70 times (1400 rev/min) in a VIRTUS PII glass homogenizer. The homogenate was centrifuged at 10,000×g, for 20 min, at 4 °C to remove cell debris. Finally, the supernatant was ultracentrifuged at 100,000×g, for 2 h, at 4 °C, using an Optima MAX-XP ultracentrifuge (Beckman Coulter, TLA 110 rotor). The ultracentrifuged pellet containing the membranes was resuspended in 1x PBS with a protease inhibitor cocktail (SIGMA-FAST^{TM}). For long-term storage, the cell membrane extracts were stored at −80 °C and used within 1 month [45]. Cell membrane extract was also characterized in size distribution and concentration by DLS, Cryo-TEM, and NTA.

2.5. Functionalization of nanoparticles with the cell membrane and EVs

After extraction, cell-derived membranes, isolated EVs, and gold nanorods were sonicated separately in an ultrasonic bath for 15 min at 4 °C and 37 Hz with 80% power (Elmasonic P). For nanoparticles functionalization, cell membranes or EVs (100 µL, 1 × 10^{11} particles mL^{-1}) were added to 1000 µL of citrate-AuNRs (optical density at 700 nm = 0.4) and sonicated with the same parameters as described above. The nanoparticles were then extruded 15 times through a 200 nm pore polycarbonate membrane (Avanti Lipids) using an Avanti mini-Extruder.

To study the effects of different AuNRs functionalization strategies on cellular uptake, gold nanorods coated with extracellular vesicles or with cell membranes (eAuNR and mAuNR, respectively) were labeled with 3,3-Dioctadecyloxacarbocyanine perchlorate (DiO, Sigma Aldrich). Briefly, after the extrusion, the coated nanoparticles were incubated for 1 h at 37 °C with DiO at 5 µg mL^{-1}. The samples were dialyzed overnight (12 kDa membrane, Sigma Aldrich) to remove excess of the unbound fluorescent probe. Zeta potential and size distribution measurements of all nanoparticles were performed using a Zetasizer Nano ZS, Malvern. The concentration of the vesicles and the nanoparticles were evaluated using NTA Nanosight NS300.

2.6. Transmission electron microscopy

For transmission electronic microscopy (TEM), 3 µL or 10 µL of the samples were deposited on copper grids for 60 s and dried with paper filter. Samples were stained with 3 µL of 2% uranyl acetate for 30 s and

again dried with paper filter. For Cryo-TEM analyses, the samples were prepared by depositing 3 μL of the sample on a copper grid, dried for 3 s with paper filter with further immersion in liquid ethane. The procedure was performed using Vitrobot Mark. The images were obtained using a JEOL 1400 and a JEM-2100 Transmission Electron Microscopes. The loading rate was estimated by dividing the total number of encapsulated nanorods by the total number of vesicles.

2.7. Fourier-transform infrared spectroscopy (FTIR)

FTIR samples were prepared by drop-casting 10 μL of the samples diluted in PBS 1x onto clean silicon substrates and dried under a reduced atmosphere. The spectra were collected using an Infrared spectrometer Nicolet 6700/GRAMS Suite, with 128 scans per sample with 4 cm^{-1} resolution from 4000 to 400 cm^{-1}.

2.8. Lipid composition estimation

The lipid composition of the vesicles was assessed by planar chromatography with flame ionization (Iatroscan MK-VI, Iatron, Japan). Lipids standards HC/WE (aliphatic hydrocarbons/ester), KET (ketones), TAG (triglycerides), FFA (free fatty acids), ALC (aliphatic alcohol-free), ST (sterol), AMPL (mobile polar lipids in ketone), and PL (phospholipids) were obtained from Sigma-Aldrich and all other chemicals and solvents were of analytical grade. RAW264.7 cell membranes and extracellular vesicles were resuspended in chloroform (Synth) after ultracentrifugation. The lipids samples were resolved in subsequent elution stages with an increase of solvent's polarity.

2.9. Cell viability

Cell viability was investigated by MTT assay after 24 h of incubation with the NRs samples. All the cells were seeded at a density of 2×10^3 cells per well in 96-well plates and grown for 24 h. Prior incubation, media was removed and 100 μL of the nanoparticles at concentrations of 1×10^8, 5×10^8, 1×10^9, and 5×10^9 particles mL^{-1} were incubated in DMEM 10% FBS (RAW264.7, L929, FC3H, HTC cells) or RPMI 10% FBS (4T1 cells). After 24 or 48 h, the nanoparticles were removed, the cells were washed with 1x PBS and 100 μL of 0.5 mg mL^{-1} 3-(4,5-dimethylthiazol-2-yl)-2,5-diphenyltetrazolium bromide (MTT, Sigma) were added with additional incubation for 3 h. Further, formazan crystals were dissolved in 100 μL of dimethyl sulfoxide (DMSO, Synth) per well and left under orbital agitation for at least 15 min. Absorbance measurements were performed at 570 and 630 nm using a microplate reader SpectraMax M3 (Molecular Devices). Cell viability was calculated compared to controls without treatment as described in Eq. (1).

$$cell\ viability(\%) = \frac{(A_{570sample} - A_{630sample})}{A_{570control} - A_{630control}} \times 100 \quad (1)$$

where $A_{570sample}$ is the absorbance at 570 nm and $A_{630sample}$ at 630 nm of treated samples, while $A_{570control}$ and $A_{630control}$ represent the absorbance of non-treated samples or controls. Data analysis was performed using Origin 2020.

2.10. Reactive oxygen species (ROS)

Reactive oxygen species (ROS) assay was carried out using 2′,7′-dichlorodihydrofluorescein diacetate (H_2DCFDA) as a probe. In 96-well plates, 2×10^3 cells per well were seeded. After 24 h, eAuNR and mAuNR (100 μL) were incubated for 24 h at two concentrations (1×10^8 and 5×10^8 particles mL^{-1}). Hydrogen peroxide (H_2O_2 – 100 μM, Merck) was used as positive control and incubated 1 h before to the end of 24 h incubation. Cells were rinsed with PBS and incubated with 50 μM of H_2DCFDA in cell culture media for 1 h at 37 °C with 5% CO_2. Fluorescence was measured at wavelengths of 485 nm (excitation) and 530 nm (emission) using a microplate reader SpectraMax M3 (Molecular Devices), after washing and adding fresh PBS to the cells. The fluorescence intensity values were normalized by the ROS fluorescence from the control.

2.11. Cellular uptake studies

2.11.1. AuNRs uptake analysis by High content Image Screening

In 96-well plates, 5×10^3 cells per well (RAW264.7, 4T1, and L929) were seeded and grown for 24 h. The medium was removed, followed by the incubation of 100 μL per well of 1×10^8 particles mL^{-1} eAuNR or mAuNR (containing DiO as the fluorescent probe) for 4 h. For inhibition studies, the agents: amiloride (100 μg mL^{-1}), nystatin (40 μg mL^{-1}), nocodazole (10 μg mL^{-1}), hydroxy-dynasore (100 μmol L^{-1}), and dansyl-cadaverine (100 μmol L^{-1}) (all from Sigma Aldrich) were incubated for 30 min prior to the incubation with the nanoparticle and not removed during the nanoparticle's incubation. After incubation, cells were washed twice with PBS, fixed with 3.7% paraformaldehyde (PFA) for 10 min, and washed 3x with PBS. A bovine serum albumin (BSA) suspension, 2% (w/v) in 100 μL was incubated for 15 min. Following, the cells were washed 3x with PBS and incubated with 4′,6-diamidino-2-phenylindole dihydrochloride (DAPI, 100 μL at 2 μg mL^{-1}) for 10 min. The samples were washed with PBS followed by one washing with distilled water. Images were acquired on ImageXpress XLS High Content Image System (Molecular Devices), with the 20× magnification lens (Plan fluor 20×/0.45), with cells immersed in 100 μL of PBS. A total of 25 images were acquired for each condition. For automatic quantitation of NPs uptake, the Transfluor module was used to create a mask able to quantify the fluorescence intensity of labeled-NPs inside the cells. The integrated intensity was normalized by nuclei count, to remove possible interferences by different cell numbers within the wells.

2.11.2. Inductively coupled plasma mass spectrometry (ICP-MS)

Internalization of the nanoparticles in RAW264.7, 4T1, and L929 cells were also evaluated with ICP-MS. In a 12-well plate, cells were seeded at 1×10^5 cells/well. After 24 h, 1 mL of 5×10^8 particles mL^{-1} in DMEM or RPMI 10% FBS were incubated for 4 h. After incubation, the medium containing the particles was removed, cells were washed twice with PBS and trypsinized or scraped. Cells were centrifuged at 800×g for 5 min, resuspended in PBS and the cell viability was evaluated with a trypan blue exclusion test. Cells were again centrifuged (800×g, 5 min) and each pellet was dissolved with 500 μL of aqua regia and further diluted in 10 mL of ultrapure water. Finally, the samples were analyzed by LabExata using NexIon 2000 from Perkin Elmer.

2.12. Confocal microscopy

The internalization of eAuNR and mAuNR in RAW264.7 and 4T1 cells was evaluated by confocal laser scanning microscopy (CLSM). The cells were incubated on glass slides, in a 24-well plate, at an initial seeding of 5×10^4 cells per well, and grown for 24 h. Further, 50 μL of the nanoparticles from a stock solution in 500 μL of medium were added over the plated cells for 4 h. LysoTracker™ Deep Red (Thermo Fisher) was incubated at 75 nmol L^{-1} for one hour before the end of incubation of the nanoparticles. Cells were washed twice with 1X PBS and fixed with 3.7% paraformaldehyde (PFA) for 10 min. Prior to the incubation with 2%(w/v) of BSA, the cells were washed twice with PBS and incubated for 15 min. DAPI was incubated at 2 μg mL^{-1} for 10 min, and then the slides were washed with PBS followed by distilled water. Slides were mounted with Fluoroshield. Image acquisition was performed on a Zeiss (LSM780) confocal microscope with water immersion (60x objective) and analyzed using Image J.

2.13. Western Blot

Samples (10 μL, containing 6×10^8 particles) were mixed with

Laemmli sample buffer, boiled at 100 °C for 5 min, loaded onto 8% acrylamide gels, and run at 100 V for 1.5 h. Gels were transferred to nitrocellulose membranes for 2 h (0.45 μm, Biorad) and blocked with 5% (w/v) bovine serum albumin (BSA) in Tris-buffered saline with 0.05% (v/v) Tween 20 (TBS-T) for 1 h. For identification of proteins, membranes were probed with primary antibodies anti-flotillin 1 (1:1000, BD, 610821), anti-CD47 (1:1000, Thermo Fischer PA5-81591) and anti-annexin 2 (1:1000, Sigma Aldrich QC5535), anti-ALIX (1:1000, Abcam Ab186429) and incubated overnight at 4 °C. The membranes were then washed four times with TBS-T (5 min each), and secondary antibodies diluted in non-fat milk were added and detected by enhanced chemiluminescence (ECL, Thermo Scientific, 32,106 and 34095). For the cell lysate obtention, 2×10^6 cells were plated overnight. Following, the cells were washed twice with 1X PBS and 15 μL of lysis buffer was added and let rest for 2 h in ice. Finally, the lysate was centrifuged (10,000×g,

4 °C) for 10 min and the supernatant was collected. A total of 10 μg of protein was loaded on gels. Images of the membranes were acquired on a molecular imager (ChemidocTM XRS; Biorad).
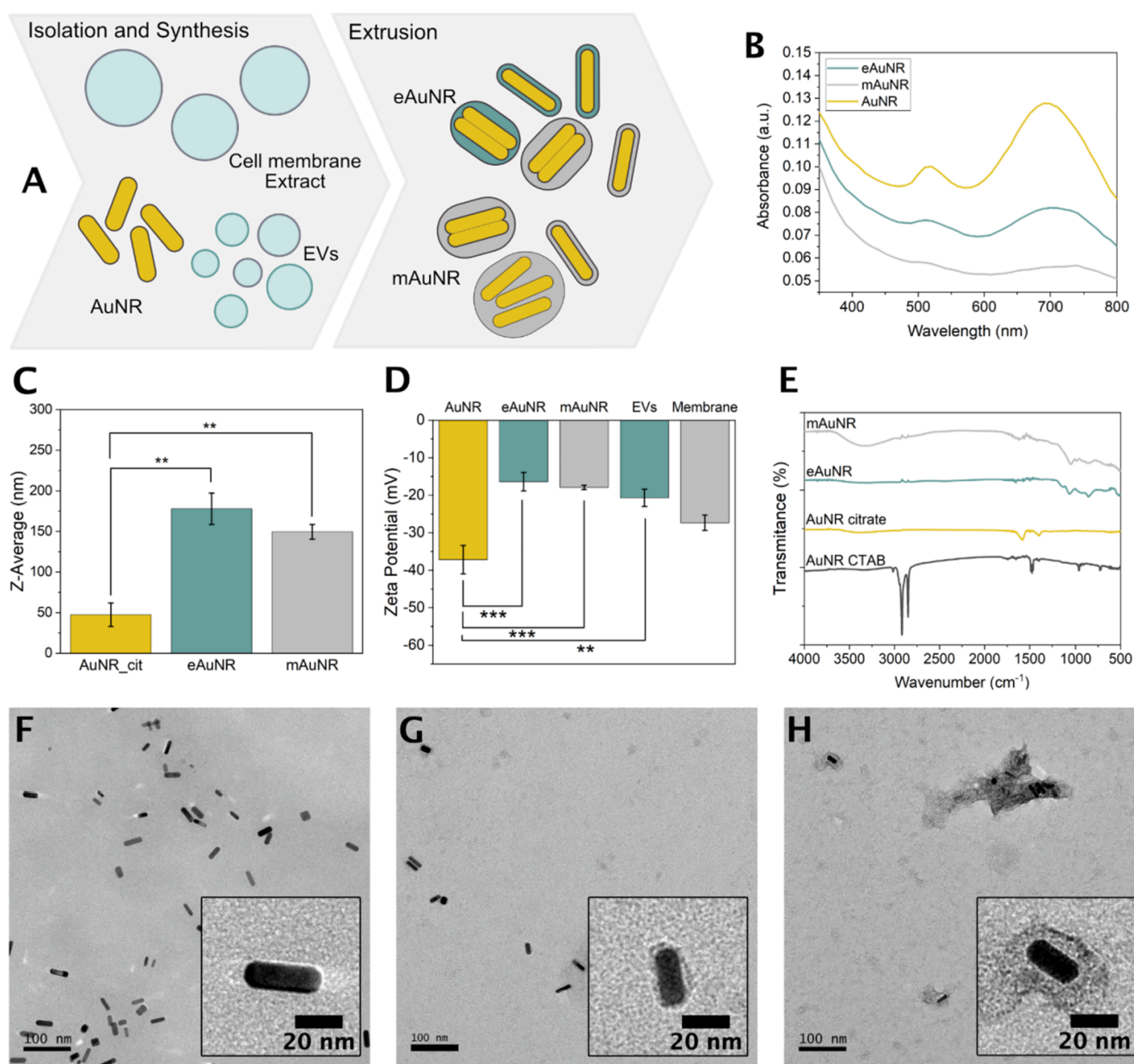
2.14. Statistical analysis

Statistical analysis was performed using Prism 9, and the test performed was one-way ANOVA with Tukey's comparisons. The measures are represented by mean and standard error.

3. Results

3.1. EVs and cell membrane characterization

The macrophage-derived EVs and the cell membrane extracts were

Fig. 2. Characterization of the gold nanorods coated with the cell membrane (mAuNR) and extracellular vesicles (eAuNR) fabricated by extrusion through a 200 nm pore size membrane. (A) Schematic view of the functionalization that resulted in different protein and lipids patterns at the nanoparticles surface. (B) UV–Vis spectra, (C) Size distribution analysis (Z-average) in one-way ANOVA with Tukey's comparisons with three independent syntheses, (D) zeta potential, and (E) FTIR spectra of eAuNR and mAuNR. TEM images with negative staining of (F) AuNR-citrate (G) eAuNR and (H) mAuNR. Scale bar: 100 nm and 20 nm (The measurements are represented by average and error bars represent the standard error of three independent syntheses, *$p < 0.05$; **$p < 0.01$; ***$p < 0.001$).

characterized by Western Blot, Cryo-TEM, NTA, and DLS (Fig. 1). Fig. 1A shows a schematic overview of EV biogenesis, distinguishing membrane and endosomal secreted vesicles. Fig. 1D shows the Cryo-TEM images of EVs isolated from RAW264.7 in which a lipid bilayer can be observed with diameter of 145 ± 40 nm, corroborating the NTA and DLS measurements (Fig. 1B). Likewise, Fig. 1E displays bilayer vesicles obtained from RAW264.7 membrane extracts with a mean diameter of 233 ± 20 nm, obtained by NTA, similar to the values obtained by DLS (Fig. 1C). The particle concentrations for isolated EVs and cell membrane extracts were $(2.1 \pm 1.2) \times 10^{11}$ and $(1.2 \pm 1.1) \times 10^{11}$ particles mL^{-1}, respectively, as measured by NTA. The protein content of EVs and membrane extracts were evaluated by Western Blot to identify the presence of CD47, flotillin 1, and annexin 2 (Fig. 1F). CD47 and Annexin 2 were detected only in the cell membranes. Flotillin 1 was present in the EVs and the cell membrane of the macrophages. The cell membrane extract exhibited a higher amount of phospholipids in comparison to the extracellular vesicles, as analyzed by planar chromatography (Fig. 1G) [47].

3.2. eAuNR and mAuNR characterization

The functionalization of the gold nanorods with the EVs or the cellular membranes was performed via extrusion using 200 nm pore size membranes, as depicted in Fig. 2A. Functionalized AuNRs showed changes in absorption, size and homogeneity characteristics, compared to their non-functionalized counterparts. The neat AuNRs displayed a typical electronic absorbance spectrum, with absorption bands at 520 and 700 nm (near-infrared region) as shown in Fig. 2B. For the functionalized NRs, a decrease in the absorption bands intensity was observed. Additionally, both eAuNR and mAuNR presented a redshift (compared to neat AuNRs), probably due to changes caused by the presence of the biological coatings in the dielectric constant in the system [23]. For mAuNR, in particular, a significant decrease in the absorption intensity was observed, due to the close proximity between gold nanorods within the vesicles, leading to plasmon coupling effects [23]. DLS and NTA measurements showed an increase in size (Fig. 2C) and a decrease in the concentration (Figure S2, Supporting information) for the vesicles-functionalized AuNR when compared to the isolated vesicles. The nanoparticles concentrations [48] were estimated by NTA as $1.4 \times 10^{11} \pm 1.6 \times 10^{10}$ and $3.4 \times 10^{11} \pm 5 \times 10^{10}$ particles mL^{-1} for eAuNR and mAuNR, respectively (Figure S2). Average sizes of 177.9 ± 19.3 nm for eAuNR (PdI 0.46 ± 0.14) and 149.5 ± 9 nm for mAuNR (PdI 0.32 ± 0.07) are observed in Fig. 2C. The zeta potential values of the as-synthesized NRs were -37.5 ± 3.8 mV (Fig. 2D), which shifted to -16.4 ± 2.4 mV for eAuNR and to -18 ± 1 mV for mAuNR, indicating the successful functionalization, since the latter values are close to those of the isolated membranes (-27.3 ± 2 mV) and EVs (-20.7 ± 2 mV).

Fig. 2E shows the FTIR spectra from AuNR_CTAB, AuNR_citrate, EVs/AuNRs (eAuNR), and cell membrane/AuNRs (mAuNR) systems. The exchange of CTAB by sodium citrate in the AuNRs could be confirmed by the decrease in the two intense bands at 3000 and 2800 cm^{-1} that correspond to the symmetric and asymmetric stretching of the methylene group from CTAB. Additionally, the presence of two bands around 1500 cm^{-1}, assigned as the stretching of carboxylate groups, confirmed the presence of citrate (AuNR_citrate). After extrusion of AuNR with EVs and cell-derived membranes, two bands at 1500 and 1350 cm^{-1} could be observed in the spectra from eAuNR and mAuNR, which correspond to the deformation modes of CH$_2$ and CH$_3$ from the lipid molecules. A band at 3400 cm^{-1}, assigned to –OH from water, was more prominent in the mAuNR samples, indicating a higher level of the hydration of the membrane when compared to eAuNR [49].

To better investigate the morphology and size of the AuNRs systems, the nanomaterials were evaluated by TEM, using negative staining (Fig. 2F-H). As shown in the TEM images of the functionalized NRs (Fig. 2G and 2H), an organic layer surrounding the rods was observed in both systems. For mAuNR samples, the TEM images revealed more AuNRs assembled within membrane vesicles when compared to eAuNR, that exhibited a more individually-coated pattern. The assembly of the gold nanorods functionalized with the cell membrane, as observed in Fig. 2H, confirms the plasmonic coupling observed in Fig. 2B, due to the decrease in intensity of the longitudinal peak. Photothermal conversion studies were also performed and revealed that the coating type do not affect the ability of the AuNRs systems to reach hyperthermia temperatures (Figure S3).

### 3.3. Toxicity studies of eAuNR and mAuNR

In vitro toxicity studies were performed to investigate the effect of different AuNRs functionalization on cell viability. Macrophage (RAW 264.7), breast tumor (4T1), and fibroblasts (L929) cell viability were assessed by MTT assay after 24 h incubation with the AuNRs systems at a concentration of 1×10^9 particles mL^{-1}. mAuNR, eAuNR and citrate induced significant toxicity in the source cells when compared to the AuNR_PEG, used as control (Fig. 3A). For 4T1 cells, no toxicity was observed for all samples, and an increase in the mitochondrial activity was observed for incubation with AuNR_citrate (Fig. 3B). Similarly, all the nanomaterials showed no statistically significant reduction in L929 cell viability (Fig. 3C).

Concentration-dependent assays were performed to analyze the differences between the eAuNR and mAuNR groups. For RAW264.7 cells, at the lowest concentration of 1×10^8 particles mL^{-1}, mAuNR caused higher toxicity when compared to eAuNR (Fig. 3D). At higher concentrations, both nanomaterials decreased cell viability in *ca.* 50%. The viability of the 4T1 and L929 cells was not affected by the presence of the AuNRs systems (Fig. 3E and 3F). Intracellular ROS generation was evaluated at two nanoparticles concentrations, as seen in Fig. 3G-I. For all cell lines, no significant differences between the nanoparticles were confirmed.

Trypan blue exclusion test was also performed on RAW264.7 and L929 to evaluate membrane damage on the cells after the exposure to different gold nanorods coating (Figure S4). The results show that for both cells the membrane is intact, and no reduced viability was observed. Additionally, viability studies in hepatic cell lines showed no toxicity for all evaluated groups (Suppl. Figures S5 and S6).

3.4. Cellular uptake assays

To understand the effects of different AuNRs coatings (EVs and cell membranes) on the toxicity profiles of the cell lines, endocytosis mechanisms were assessed using pharmacological inhibitors for the main endocytic pathways of nanoparticles (Fig. 4). Cellular uptake was evaluated using fluorescence-based techniques. The nanoparticles were labeled with DiO, a fluorescent probe that internalizes in the lipid bilayer of the vesicles. As uptake inhibitors, we used nystatin, amiloride, hydroxy-dynasore, nocodazole and dansyl-cadaverine, that inhibits caveolae, macropinocytosis, dynamin, microtubules, and clathrin-dependent endocytosis, respectively. In the source cell, RAW264.7, eAuNR uptake (Fig. 4A) was inhibited by hydroxy-dynasore, whereas the mAuNR uptake (Fig. 4E) was inhibited by amiloride, hydroxy-dynasore, and nocodazole. For metastatic breast cancer cells, eAuNR uptake (Fig. 4B) was inhibited by amiloride and hydroxy-dynasore. mAuNR internalization in 4T1 (Fig. 4F) was not influenced by these inhibitors. In the L929 cells, eAuNR internalization was decreased by hydroxy-dynasore and mAuNR uptake was also decreased by the same inhibitor, and by dansyl-cadaverine. Protein content assay (Fig. 4D) showed the presence of ALIX in both cell lysates and vesicles. Differences in the CD47 expression in cells were observed, in which 4T1 exhibited the higher CD47 expression among the cell's lysates. ICP-MS results (Fig. 4H) revealed the reduced cellular uptake of the EVs- or cell membrane-coated AuNRs by the RAW264.7 in comparison to the bare nanoparticles. As expected, internalization was higher in the macrophages. Upon normalizing the ICP-MS analysis with the gold content of
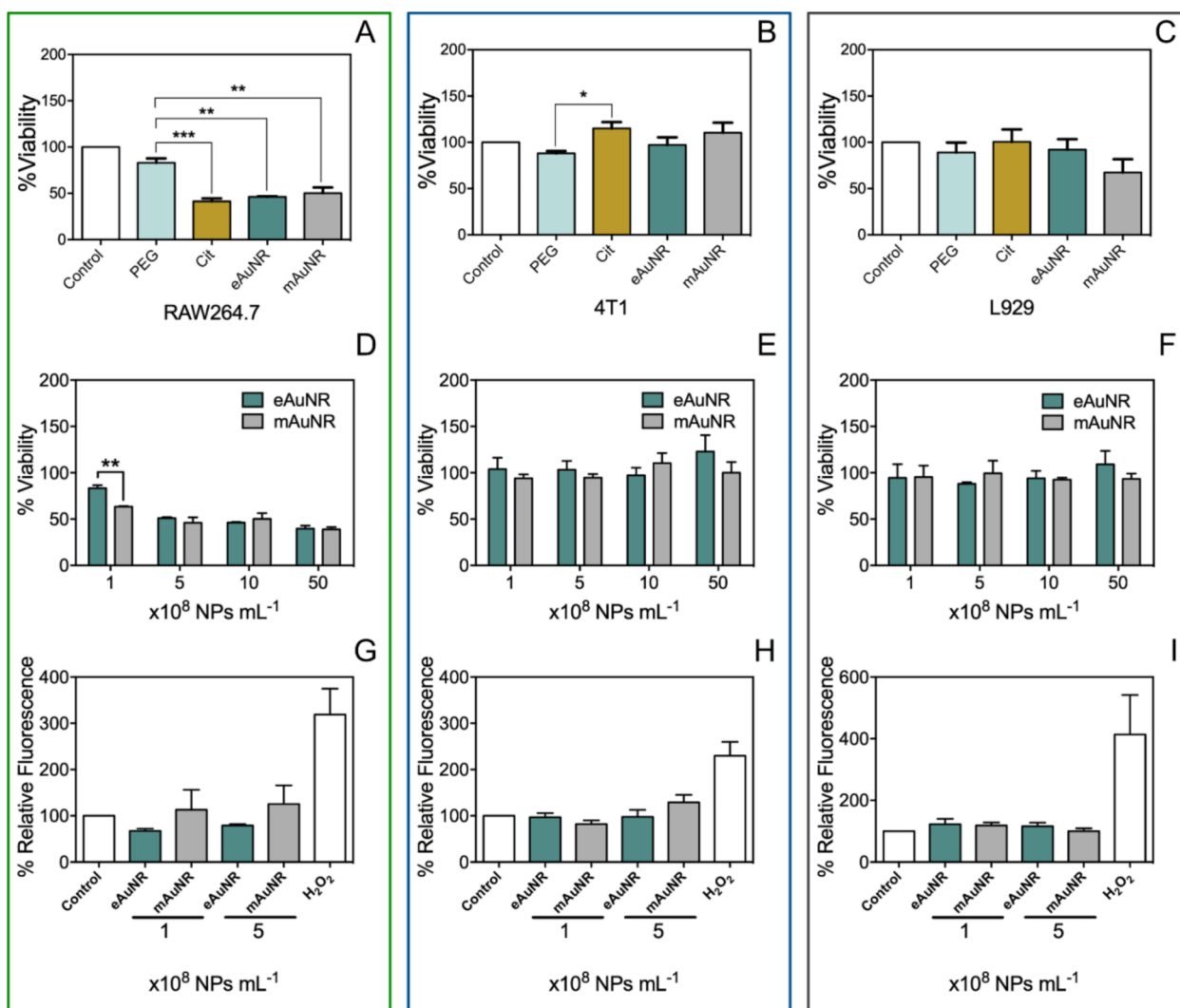
Fig. 3. Toxicity studies of the nanoparticles using RAW264.7, 4T1, and L929 cell lines. Cell viability of (A) RAW 264.7 (green), (B) 4T1 (blue) and (C) L929 (black) after 24 h incubation with the nanomaterials functionalized with PEG, citrate, EVs, and the cell membrane at a concentration of 1×10^9 particles mL^{-1}. Concentration-dependent experiments of eAuNR and mAuNR (1×10^8 to 5×10^9 particles mL^{-1}) D) RAW264.7, (E) 4T1 and (F) L929. ROS studies at the lowest tested concentrations of eAuNr and mAuNR G) RAW264.7, (H) 4T1 I) L929 cell lines. (Statistical analysis was performed using one-way ANOVA with Tukey's comparisons, MTT measurements are represented by average and error bars represent the standard error, ROS measurements are represented as the average normalized by the control and error bar by the standard error, * $p < 0.05$; **$p < 0.01$; ***$p < 0.001$). Three independent experiments were performed for each cell line. (For interpretation of the references to colour in this figure legend, the reader is referred to the web version of this article.)

the nanoparticles (Figure S7) we observe a tendency for eAuNRs to deliver more gold to all cells than the mAuNRs, as well as an increased uptake in RAW264.7 and 4T1 cell lines. Additionally, cellular uptake differences were quantitatively evaluated by High Content Image Screening and flow cytometry (Figure S8). The preferential uptake of eAuNR in the RAW264.7 is shown, and for this technique, no difference in the uptake of eAuNR and mAuNR by the 4T1 and L929 was observed.

Internalization studies were also carried out by confocal laser scanning microscopy (Fig. 5 and Figures S9 and S10). The images show a preferential uptake of eAuNR rather than mAuNR in the source cell (RAW264.7), and the opposite was observed for the breast cancer cell line. In 4T1 we observe an increased uptake of mAuNR compared to eAuNR, and a tendency to colocalize with Lysotracker also shown in Fig. 5.

4. Discussion

The advantage of using macrophage-derived EVs and membranes for NPs coating lies in the biorecognition features and reduced

immunostimulation provided by such camouflage, minimizing internalization by the source cells (macrophages), and increasing the chances of internalization by the target cancer cells [31,50]. We successfully obtained two classes of coated nanorods using EVs and cell membrane extracts of RAW264.7. We initially investigated the physico-chemical characteristics and differences in yield, structure, lipid content and protein markers of the EVs and cell membranes (Fig. 1). Nanotracking analysis showed that the isolation protocol provided a high yield of vesicles. Moreover, size distribution analysis showed that EVs are slightly smaller than the membrane vesicles, which was also confirmed by cryo-TEM analyses (Fig. 1C and 1D). The lipid content reveals that the EVs are mostly from endosomal origin [51,52], since they presented lower percentage of phospholipids in their composition, compared to the cell membranes (Fig. 1G). The EVs origin was also endorsed by the absence of the tetraspanin CD47 in WB, related to its endosomal biogenesis, in which there is an inversion of the lipid bilayer and alteration of the expressed proteins [53]. CD47 tetraspanin is a cell surface receptor present in the membrane of tumor cells that modulates immune response and inhibits phagocytosis by immune system cells
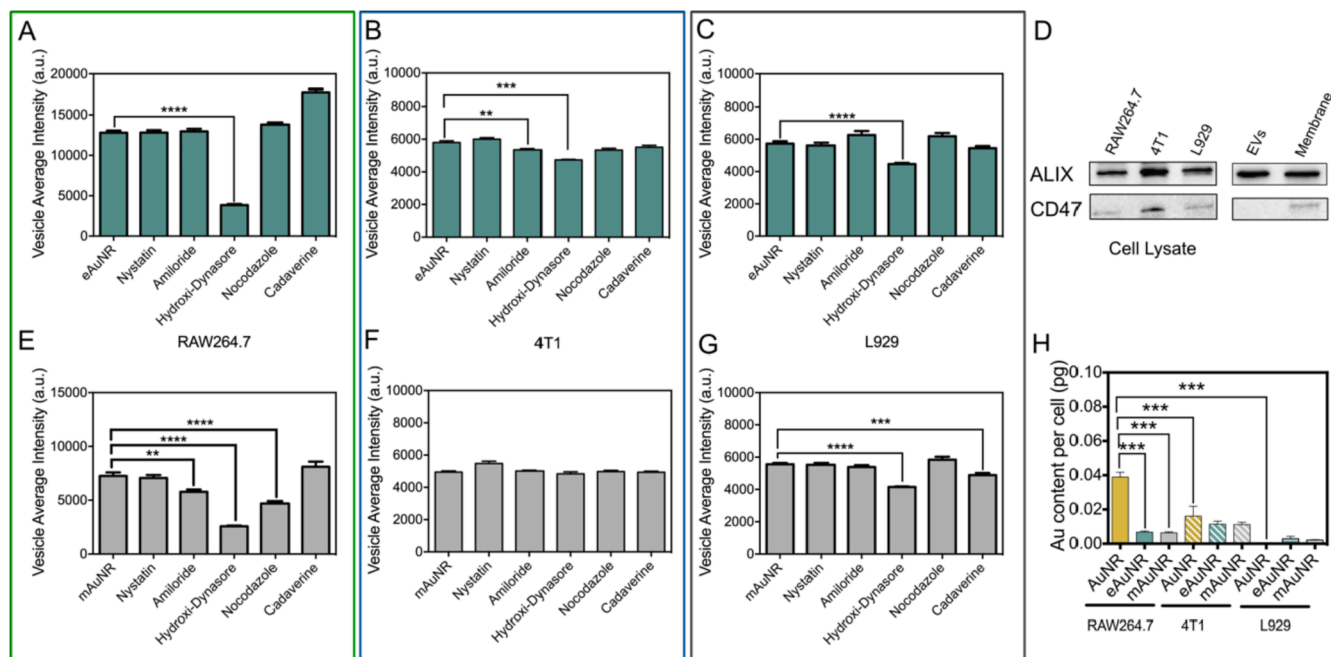
Fig. 4. Cellular uptake analyses for eAuNR and mAuNR. Endocytosis studies of eAuNR at 1×10^8 particles mL^{-1} labeled with DiO after 4 h incubation with (A) RAW264.7 (green, n = 3), (B) 4T1 (blue, n = 3) and (C) L929 (black, n = 3) cells at 37 °C in 5% CO_2 atmosphere. Internalization studies for mAuNR at $1*10^8$ particles mL^{-1} also labeled with DiO after 4 h incubation with (E) RAW264.7 (green, n = 3), (F) 4T1 (blue, n = 3) and G) L929 (black, n = 3) cells at 37 °C 5% CO_2 atmosphere. The concentration used for amiloride, nystatin, nocodazole, hydroxy-dynasore, and cadaverine were 100 μg mL^{-1}, 40 μg mL^{-1}, 10 μg mL^{-1}, 100 μmol L^{-1}, 100 μmol L^{-1} respectively. (D) Protein content of EVs and membrane extract with cell lysates estimated via Western Blot to identify the presence of CD47 and ALIX. (H) Internalization analysis by determining the glod content via ICP-MS in RAW264.7, 4T1 and L929 incubating the nanoparticles at 5×10^8 particles mL^{-1} for 4 h (Statistical analysis using one-way ANOVA with Tukey's comparisons, measurements are represented by average and error bars represent the standard error, * $p <$ 0.05; **$p < 0.01$; ***$p < 0.001$; **** $p < 0.0001$). (For interpretation of the references to colour in this figure legend, the reader is referred to the web version of this article.)

[17,54]. Flotillin 1 has a crucial role in the production of EVs and is widely explored as an EVs marker [38], explaining the expression of this marker in the cell extracts and in the EVs [55]. The presence of residual cytoplasmic molecules, as Annexin 2 (Fig. 1F) in the cell membrane vesicles is expected, due to the protocol of isolation by hypotonic and lysis buffer [56]. These observations are important to understand the differential delivery and internalization abilities of these nanomaterials, since their biophysical properties can be altered upon interaction with the cells [57]. Fig. 2 shows the efficient functionalization of AuNRs with vesicles and membranes. In addition, extrusion was shown to be an important step for the effective coating of the nanorods (Figure S1, Supporting information). The mAuNR nanoparticles exhibited more aggregates than the eAuNR system, in which the loading rate was 2.5 and 2.1 nanorods/vesicles respectively.

Toxicity assays revealed the effects of the AuNRs against the RAW264.7 source cells (Fig. 3), due to the more effective internalization of the nanomaterials in this cell line (Fig. 4H). mAuNR, eAuNR, and AuNRs_citrate were highly toxic for RAW264.7, whereas AuNR_PEG showed no reduction in cell viability (Fig. 3A), which was attributed to the presence of PEG, that prevents identification and further uptake by cells of the immune system [58]. At the lowest concentration, mAuNR particles exhibited higher toxicity against the macrophages, in comparison to the eAuNR particles, which may be and indicative of distinct uptake pathways (Fig. 4) [59]. Incubation with AuNR_citrate did not induce toxicity to 4T1 cells, and an increase in the mitochondrial activity of the cells was observed, probably because citrate is an important molecule in the biochemical pathways for cells energy production [60]. No significant differences were observed between the nanoparticles in L929. Trypan blue exclusion tests did not show membrane damage after 24 h of exposure (Figure S4).

Intracellular ROS detection experiments revealed that there was no oxidative stress in cells (RAW 264.7, 4T1, and L929) upon treatment

with nanorods functionalized with PEG, citrate, EVs, or cell membrane. The internalization of gold nanorods did not necessarily raised ROS levels to the point of generating oxidative stress [61].

The endocytosis studies explored whether the differences in the nanorod's bio-coatings could lead to different internalization pathways (Fig. 4). By using different uptake inhibitors, we found that eAuNR internalization is governed by dynamin-dependent endocytosis in all cell lines, since the internalization was significantly affected by the addition of hydroxi-dynasore in the three cell lines [62]. During EVs biogenesis in multivesicular bodies, these vesicles are fully enriched with several cell receptors, such as integrins, tetraspanins, among others. These molecules are important to reach and internalize target cells after secretion to the extracellular medium. Dynamin-dependent endocytosis is mediated by several cell surface receptors, for example, heparan sulfate proteoglycan and galectin-5, explaining why EVs would be preferentially internalized through this pathway [62,63]. In 4T1 cells, in particular, macropinocytosis was also shown to be an important endocytosis pathway for eAuNR [64]. By inhibiting the clathrin-dependent endocytosis, the uptake of the nanoparticles increased, showing a cross-regulation between the endocytic mechanisms [65]. Additionally, eAuNR interacted more with the source cell in comparison to the other cell lines.

For mAuNR in RAW264.7 cells, the endocytosis was driven by macropinocytosis, dynamin, and microtubules pathways (Fig. 4E). Clathrin-dependent inhibition also increased for mAuNR, as a cross-regulation mechanism from the macrophage to compensate the deformations in the cell membrane by the inhibitor. Importantly, the metastatic breast cancer cells (4T1) internalized the mAuNR by another mechanism [66], since uptake did not decreased using the chosen inhibitors. The healthy cell line, L929, endocytosed the mAuNR via clathrin.

Differences in the uptake pathways can be explained by the different
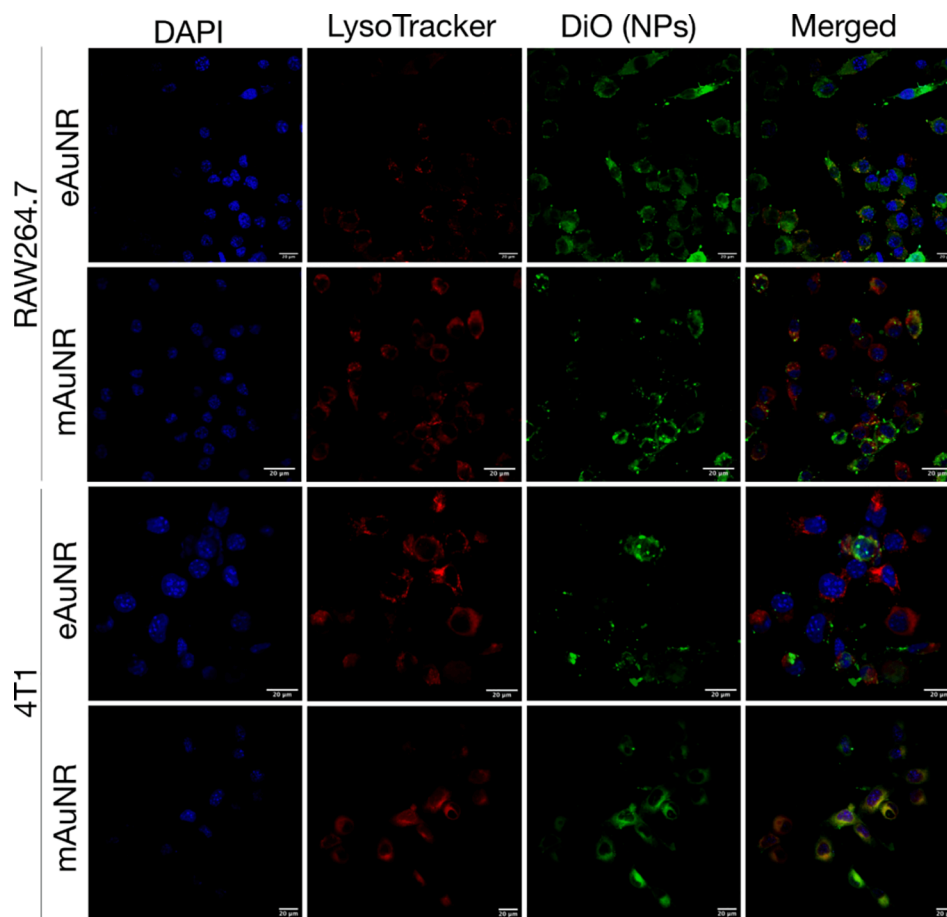
Fig. 5. Cellular uptake analysis by confocal laser scanning microscopy of RAW264.7 and 4T1 treated with eAuNR and mAuNR with DiO at the same initial fluorescence intensity for 4 h. The images were taken with a 60× water immersion objective lens. Scale bar = 20 μm.

protein content in the cells and in the nanoparticles (Fig. 4D). The increased uptake of the eAuNR by the source cells can be related to the lack of CD47 expression [22]. It is important to note the higher expression of CD47 in 4T1 in comparison to the other cell lines, as revealed by the Western Blot results, which are in agreement with the tetraspanin-driven pathway to internalize mAuNR, which is dependent on actin filaments (Fig. 4F) [66]. This homotypic adhesion is one of the mechanisms of metastatic tumor development and commonly presented in cell membrane-coated nanoparticles [21,29,67].

ICP-MS analysis (Fig. 4H) showed that the functionalization of gold nanorods with the vesicles decreased the uptake by the macrophages at the same nanoparticle concentration, however, no statistical differences were observed between eAuNR and mAuNR [68]. These results associated with the viability assays and at concentrations above 5×10^8 particles mL^{-1} show that the toxicity levels might be associated with the amount of gold delivered. ALIX expression in cells is known to preferentially characterize the internalization of molecules via clathrin-independent endocytosis [69]. Additionally, this marker is used for characterization of small EVs because it is related to endosomal pathways [38]. In our inhibition assays, the clathrin-mediated endocytosis only accounted for a small portion of internalization in L929 for mAuNR, and ALIX expression is similar for all cell lysates. Interestingly, normalized ICP-MS results revealed that eAuNR delivered more gold nanorods than mAuNR (Figure S5). Confocal laser scanning microscopy confirmed the differences in cell uptake, revealing the higher uptake of eAuNR in the RAW264.7 when compared to mAuNR. The opposite occurred for the 4T1 cells. (Fig. 5).

Many studies have shown that EVs play a role in the microenvironment of tumours [34,50,70] being described as useful tools for drug

delivery [34,71]. Cell membrane nanoparticles have also been extensively reported to be an excellent delivery tool to actively target the tumor site [25–27]. However, to our knowledge, a comparison between these bio-coatings in terms of cell toxicity and internalization processes has not been reported. Our findings point out CD47 as a crucial marker for the main difference observed in the uptake mechanisms. The differences regarding the two coatings studied here might be related to the CD47-SIRPα present in mAuNR, as a 'do not eat me' sign for macrophages and as 'eat me' for metastatic tumor cells (homotypic binding) (Fig. 6) [22]. Other important difference between the coatings is their lipid content (cell membranes contained more phospholipids than the EVs), which may contribute to the different uptake mechanisms. In general, the higher the amount of phospholipids, the higher the number of zwitterionic groups, leading to a lower uptake by macrophages [72].

In a paper by Kanada et al., the authors compared EVs from endosomal origin with microvesicles derived from plasma membrane. They showed that delivery was more efficient using the microvesicles [33]. The latter study, however, did not address the influence of CD47, nor of the lipid contents. In another study, Belhadj et al. evaluated the uptake of EVs obtained from different source cells. The authors concluded that the absence of CD47 in specific EVs was the main parameter responsible for their uptake by macrophages, similarly to what we observed here [23]. Together, our findings showed the importance to consider CD47 in the composition of extracellular vesicles characterization in nanomaterials design. Our results can be used for future investigations exploring nanomaterials developed for specific cell types or diseases.
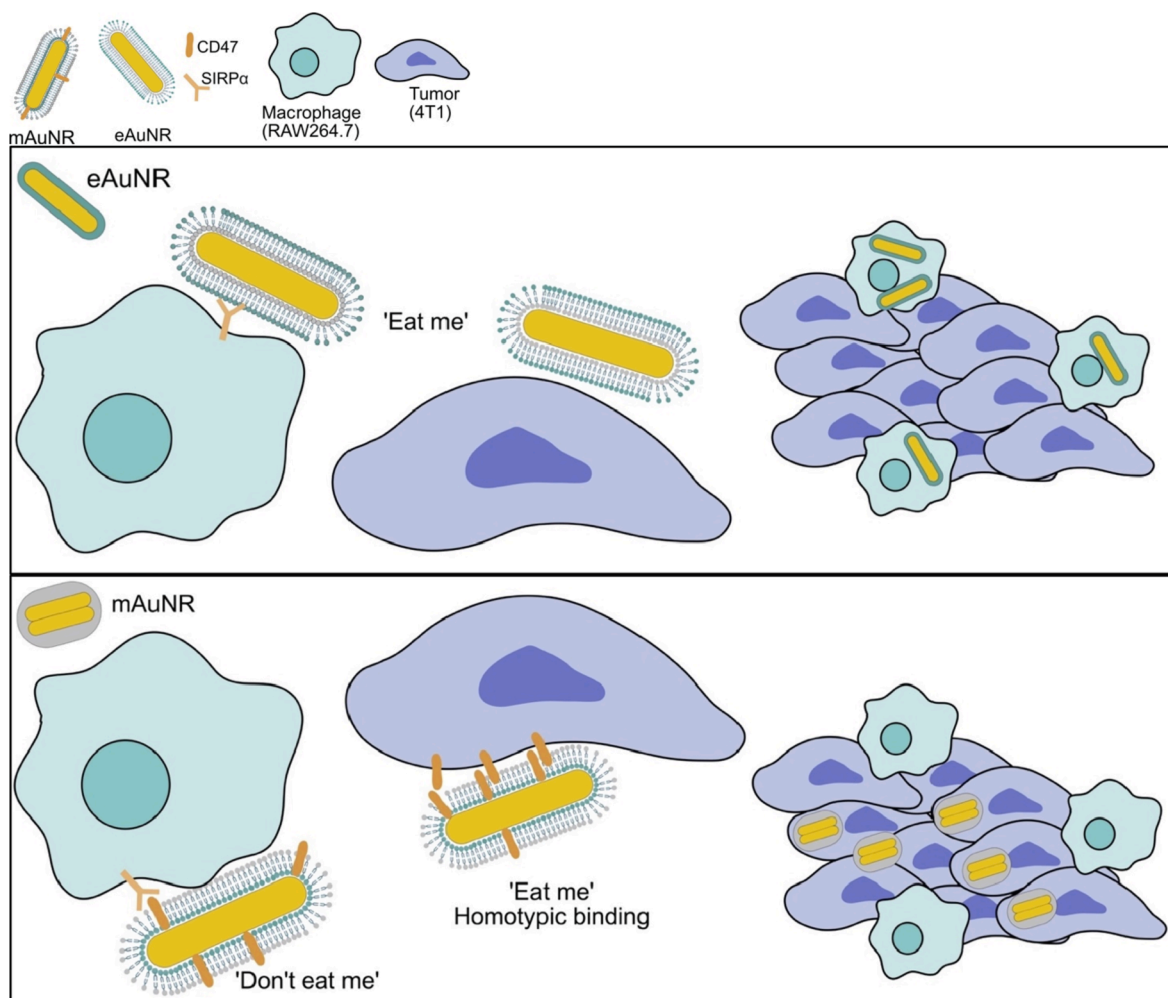
Fig. 6. Schematic of internalization pathway and differences in the eAuNR and mAuNR interaction for cancer treatment.

5. Conclusions

AuNRs covered with macrophage derived EVs or cell membranes were synthesized, and their cell internalization features had been compared using cell lines related with different tumor microenvironment. The main difference between these biomimetic coatings was related to CD47, which absence in the EVs was shown to be a key parameter for their internalization by the source cells, but not by the metastatic cell lines. The presence of CD47 in the cell membrane allowed a pronounced internalization in metastatic cancer cells. The delivery of the AuNRs to the metastatic breast cancer cells (4T1) was more efficient for cell membrane-coated nanorods (mAuNRs systems) in comparison to the EVs-coated gold nanorods. Thus, we recommend a detailed characterization regarding the presence or absence of CD47 in the EVs- based nanomaterials for cancer therapy. The results presented here shine light towards the understanding of the role of EVs in cellular communication for their use as delivery tools, when compared to cell membrane-covered nanoparticles.

Credit authorship contribution statement

Paula Maria Pincela Lins: Conceptualization, Methodology, Writing – original draft, Writing – review & editing. **Laís Ribovski:** Methodology, Writing – original draft, Writing – review & editing. **Luana Corsi Antonio:** Methodology, Writing – review & editing. **Wanessa Fernanda Altei:** Methodology, Writing – review & editing. **Heloisa Sobreiro Selistre-de-Araújo:** Methodology, Writing – review & editing. **Juliana Cancino-Bernardi:** Conceptualization, Writing – original draft, Writing – review & editing. **Valtencir Zucolotto:** Conceptualization, Writing – original draft, Writing – review & editing.

Declaration of Competing Interest

The authors declare that they have no known competing financial interests or personal relationships that could have appeared to influence the work reported in this paper.

Acknowledgments

Appendix A. Supplementary material

Supplementary data to this article can be found online at https://doi.org/10.1016/j.ejpb.2022.05.018.

References

[1] A. Roy, S.D. Li, Modifying the Tumor Microenvironment Using Nanoparticle Therapeutics, Wiley Interdiscip. Rev. Nanomedicine Nanobiotechnology 8 (6) (2016) 891–908, https://doi.org/10.1002/wnan.1406.

[2] I.J. Fidler, The Pathogenesis of Cancer Metastasis: The "seed and Soil" Hypothesis Revisited, Nat. Rev. Cancer 3 (6) (2003) 453–458, https://doi.org/10.1038/nrc1098.

[3] D.F. Quail, J.A. Joyce, Microenvironmental Regulation of Tumor Progression and Metastasis, Nat. Med. 19 (11) (2013) 1423–1437, https://doi.org/10.1038/nm.3394.

[4] Z. Zhang, W.R. Karthaus, Y.S. Lee, V.R. Gao, C. Wu, J.W. Russo, M. Liu, J.M. Mota, W. Abida, E. Linton, E. Lee, S.D. Barnes, H.A. Chen, N. Mao, J. Wongvipat, D. Choi, X. Chen, H. Zhao, K. Manova-Todorova, E. de Stanchina, M.E. Taplin, S.P. Balk, D. E. Rathkopf, A. Gopalan, B.S. Carver, P. Mu, X. Jiang, P.A. Watson, C.L. Sawyers, Tumor Microenvironment-Derived NRG1 Promotes Antiandrogen Resistance in Prostate Cancer, Cancer Cell 38 (2) (2020) 279–296.e9, https://doi.org/10.1016/j.ccell.2020.06.005.

[5] T.L. Whiteside, The Tumor Microenvironment and Its Role in Promoting Tumor Growth, Oncogene 27 (45) (2008) 5904–5912, https://doi.org/10.1038/onc.2008.271.

[6] Q. Chen, G. Liu, S. Liu, H. Su, Y. Wang, J. Li, C. Luo, Remodeling the Tumor Microenvironment with Emerging Nanotherapeutics, Trends Pharmacol. Sci. 39 (1) (2018) 59–74, https://doi.org/10.1016/j.tips.2017.10.009.

[7] Y. Shi, R. van der Meel, X. Chen, T. Lammers, The EPR Effect and beyond: Strategies to Improve Tumor Targeting and Cancer Nanomedicine Treatment Efficacy, Theranostics 10 (17) (2020) 7921–7924, https://doi.org/10.7150/thno.49577.

[8] H. Kang, S. Rho, W.R. Stiles, S. Hu, Y. Baek, D.W. Hwang, S. Kashiwagi, M.S. Kim, H.S. Choi, Size-Dependent EPR Effect of Polymeric Nanoparticles on Tumor Targeting, Adv. Healthc. Mater. 9 (1) (2020) 8–15, https://doi.org/10.1002/adhm.201901223.

[9] Y. Ding, Y. Xu, W. Yang, P. Niu, X. Li, Y. Chen, Z. Li, Y. Liu, Y. An, Y. Liu, W. Shen, L. Shi, Investigating the EPR Effect of Nanomedicines in Human Renal Tumors via Ex Vivo Perfusion Strategy, Nano Today 35 (2020), 100970, https://doi.org/10.1016/j.nantod.2020.100970.

[10] S. Wilhelm, A.J. Tavares, Q. Dai, S. Ohta, J. Audet, H.F. Dvorak, W.C.W. Chan, Analysis of Nanoparticle Delivery to Tumours, Nat. Rev. Mater. 1 (2016) 16014, https://doi.org/10.1038/natrevmats.2016.14.

[11] Y.-H. Cheng, C. He, J.E. Riviere, N.A. Monteiro-Riviere, Z. Lin, Meta-Analysis of Nanoparticle Delivery to Tumors Using a Physiologically Based Pharmacokinetic Modeling and Simulation Approach, ACS Nano 14 (3) (2020) 3075–3095, https://doi.org/10.1021/acsnano.9b08142.

[12] A.E. Nel, L. Mädler, D. Velegol, T. Xia, E.M.V. Hoek, P. Somasundaran, F. Klaessig, V. Castranova, M. Thompson, Understanding Biophysicochemical Interactions at the Nano-Bio Interface, Nat. Mater. 8 (7) (2009) 543–557, https://doi.org/10.1038/nmat2442.

[13] A. Salvati, A.S. Pitek, M.P. Monopoli, K. Prapainop, F.B. Bombelli, D.R. Hristov, P. M. Kelly, C. Åberg, E. Mahon, K.A. Dawson, Transferrin-Functionalized Nanoparticles Lose Their Targeting Capabilities When a Biomolecule Corona Adsorbs on the Surface, Nat. Nanotechnol. 8 (2) (2013) 137–143, https://doi.org/10.1038/nnano.2012.237.

[14] R.H. Fang, A.V. Kroll, W. Gao, L. Zhang, Cell Membrane Coating Nanotechnology, Adv. Mater. 30 (23) (2018) 1–34, https://doi.org/10.1002/adma.201706759.

[15] C.M.J. Hu, R.H. Fang, B.T. Luk, K.N.H. Chen, C. Carpenter, W. Gao, K. Zhang, L. Zhang, "Marker-of-Self" Functionalization of Nanoscale Particles through a Top-down Cellular Membrane Coating Approach, Nanoscale 5 (7) (2013) 2664–2668, https://doi.org/10.1039/c3nr00015j.

[16] E. Sick, A. Jeanne, C. Schneider, S. Dedieu, K. Takeda, L. Martiny, CD47 Update: A Multifaceted Actor in the Tumour Microenvironment of Potential Therapeutic Interest, Br. J. Pharmacol. 167 (7) (2012) 1415–1430, https://doi.org/10.1111/j.1476-5381.2012.02099.x.

[17] P.A. Oldenborg, A. Zhelexnyak, Y.F. Fang, C.F. Lagenaur, H.D. Gresham, F. P. Lindberg, Role of CD47 as a Marker of Self on Red Blood Cells, Science (80-.) 288 (5473) (2000) 2051–2054, https://doi.org/10.1126/science.288.5473.2051.

[18] T. Deuse, X. Hu, S. Agbor-Enoh, M.K. Jang, M. Alawi, C. Saygi, A. Gravina, G. Tediashvili, V.Q. Nguyen, Y. Liu, H. Valantine, L.L. Lanier, S. Schrepfer, The SIRPα-CD47 Immune Checkpoint in NK Cells, J. Exp. Med. 218 (3) (2021), https://doi.org/10.1084/JEM.20200839.

[19] M.P. Chao, I.L. Weissman, R. Majeti, The CD47-SIRPα Pathway in Cancer Immune Evasion and Potential Therapeutic Implications, Curr. Opin. Immunol. 24 (2) (2012) 225–232, https://doi.org/10.1016/j.coi.2012.01.010.

[20] S. Kamerkar, V.S. Leblue, H. Sugimoto, S. Yang, C.F. Ruivo, S.A. Melo, J.J. Lee, R. Kalluri, Exosomes Facilitate Therapeutic Targeting of Oncogenic KRAS in Pancreatic Cancer, Nature 546 (7659) (2017) 498–503, https://doi.org/10.1038/nature22341.

[21] H. Zhao, J. Wang, X. Kong, E. Li, Y. Liu, X. Du, Z. Kang, Y. Tang, Y. Kuang, Z. Yang, Y. Zhou, Q. Wang, CD47 Promotes Tumor Invasion and Metastasis in Non-Small Cell Lung Cancer, Sci. Rep. 6 (2016) 1–11, https://doi.org/10.1038/srep29719.

[22] Z. Belhadj, B. He, H. Deng, S. Song, H. Zhang, X. Wang, W. Dai, Z.Q.A. Combined, "Eat Me/Don't Eat Me" Strategy Based on Extracellular Vesicles for Anticancer Nanomedicine, J. Extracell. Vesicles 9 (1) (2020), https://doi.org/10.1080/20013078.2020.1806444.

[23] V.S. Marangoni, J. Cancino Bernardi, I.B. Reis, W.J. Fávaro, V. Zucolotto, Photothermia and Activated Drug Release of Natural Cell Membrane Coated

[24] C.-M.-J. Hu, L. Zhang, S. Aryal, C. Cheung, R.H. Fang, L. Zhang, Erythrocyte Membrane-Camouflaged Polymeric Nanoparticles as a Biomimetic Delivery Platform, Proc. Natl. Acad. Sci. 108 (27) (2011) 10980–10985, https://doi.org/10.1073/pnas.1106634108.

[25] Q. Zhang, A. Honko, J. Zhou, H. Gong, S.N. Downs, J.H. Vasquez, R.H. Fang, W. Gao, A. Griffiths, L. Zhang, Cellular Nanosponges Inhibit SARS-CoV-2 Infectivity, Nano Lett. 20 (7) (2020) 5570–5574, https://doi.org/10.1021/acs.nanolett.0c02278.

[26] J. Jin, B. Krishnamachary, J.D. Barnett, S. Chatterjee, D. Chang, Y. Mironchik, F. Wildes, E.M. Jaffee, S. Nimmagadda, Z.M. Bhujwalla, Human cancer cell membrane-coated biomimetic nanoparticles reduce fibroblast-mediated invasion and metastasis and induce T-cells, ACS Appl. Mater. Interfaces (2019) 7850–7861, https://doi.org/10.1021/acsami.8b22309.

[27] L. Rao, G.T. Yu, Q.F. Meng, L.L. Bu, R. Tian, L.S. Lin, H. Deng, W. Yang, M. Zan, J. Ding, A. Li, Cancer cell membrane-coated nanoparticles for personalized therapy in patient-derived xenograft models, Adv. Funct. Mater. 29 (51) (2019) 1–10, https://doi.org/10.1002/adfm.201905671.

[28] Q. Jiang, Y. Liu, R. Guo, X. Yao, S. Sung, Z. Pang, W. Yang, Erythrocyte-Cancer Hybrid Membrane-Camouflaged Melanin Nanoparticles for Enhancing Photothermal Therapy Efficacy in Tumors, Biomaterials 192 (2019) 292–308, https://doi.org/10.1016/j.biomaterials.2018.11.021.

[29] H. Sun, J. Su, Q. Meng, Q. Yin, L. Chen, W. Gu, P. Zhang, Z. Zhang, H. Yu, S. Wang, Y. Li, Cancer-Cell-Biomimetic Nanoparticles for Targeted Therapy of Homotypic Tumors, Adv. Mater. 28 (43) (2016) 9581–9588, https://doi.org/10.1002/adma.201602173.

[30] D. De Pasquale, A. Marino, C. Tapeinos, C. Pucci, S. Rocchiccioli, E. Michelucci, F. Finamore, L. McDonnell, A. Scarpellini, S. Lauciello, M. Prato, A. Larrañaga, F. Drago, G. Ciofani, Homotypic Targeting and Drug Delivery in Glioblastoma Cells through Cell Membrane-Coated Boron Nitride Nanotubes, Mater. Des. 192 (2020), 108742, https://doi.org/10.1016/j.matdes.2020.108742.

[31] M. Xuan, J. Shao, L. Dai, J. Li, Q. He, Macrophage Cell Membrane Camouflaged Au Nanoshells for in Vivo Prolonged Circulation Life and Enhanced Cancer Photothermal Therapy, ACS Appl. Mater. Interfaces 8 (15) (2016) 9610–9618, https://doi.org/10.1021/acsami.6b00853.

[32] M. Tkach, C. Théry, Communication by Extracellular Vesicles: Where We Are and Where We Need to Go, Cell 164 (6) (2016) 1226–1232, https://doi.org/10.1016/j.cell.2016.01.043.

[33] M. Kanada, M.H. Bachmann, J.W. Hardy, D. Omar, L. Bronsart, A. Wang, M. D. Sylvester, T.L. Schmidt, R.L. Kaspar, M.J. Butte, A.C. Matin, D.O. Frimannson, L. Bronsart, A. Wang, M.D. Sylvester, T.L. Schmidt, R.L. Kaspar, M.J. Butte, A. C. Matin, C.H. Contag, Differential fates of biomolecules delivered to target cells via extracellular vesicles, Proc. Natl. Acad. Sci. 112 (12) (2015), https://doi.org/10.1073/pnas.1418401112.

[34] W. Nie, G. Wu, J. Zhang, L.-L.-L. Huang, J. Ding, A. Jiang, Y. Zhang, Y. Liu, J. Li, K. Pu, H.-Y.-Y. Xie, Responsive Exosome Nano-Bioconjugates for Synergistic Cancer Therapy, Angew. Chemie Int. Ed. 59 (5) (2020) 2018–2022, https://doi.org/10.1002/anie.201912524.

[35] P. Lara, S. Palma-Florez, E. Salas-Huenuleo, I. Polakovicova, S. Guerrero, L. Lobos-Gonzalez, A. Campos, L. Muñoz, C. Jorquera-Cordero, M. Varas-Godoy, J. Cancino, E. Arias, J. Villegas, L.J. Cruz, F. Albericio, E. Araya, A.H. Corvalan, A.F.G. Quest, M.J. Kogan, Gold nanoparticle based double-labeling of melanoma extracellular vesicles to determine the specificity of uptake by cells and preferential accumulation in small metastatic lung tumors, J. Nanobiotechnology 18 (1) (2020) 1–17, https://doi.org/10.1186/s12951-020-0573-0.

[36] P. Lara, A.B. Chan, L.J. Cruz, A.F.G. Quest, M.J. Kogan, Exploiting the natural properties of extracellular vesicles in targeted delivery towards specific cells and tissues, Pharmaceutics 12 (11) (2020) 1–25, https://doi.org/10.3390/pharmaceutics12111022.

[37] L. Yuan, Y. Liu, Y. Qu, L. Liu, H. Li, Exosomes Derived from Microrna-148b-3p-Overexpressing Human Umbilical Cord Mesenchymal Stem Cells Restrain Breast Cancer Progression, Front. Oncol. 9 (2019) 1–14, https://doi.org/10.3389/fonc.2019.01076.

[38] C. Théry, K.W. Witwer, E. Aikawa, M.J. Alcaraz, J.D. Anderson, R. Andriantsitohaina, A. Antoniou, T. Arab, F. Archer, G.K. Atkin-Smith, D.C. Ayre, et al., Minimal Information for Studies of Extracellular Vesicles 2018 (MISEV2018): A Position Statement of the International Society for Extracellular Vesicles and Update of the MISEV2014 Guidelines, J. Extracell. Vesicles 7 (1) (2018), https://doi.org/10.1080/20013078.2018.1535750.

[39] M.A. Antonyak, R.A. Cerione, Emerging Picture of the Distinct Traits and Functions of Microvesicles and Exosomes, Proc. Natl. Acad. Sci. USA 112 (12) (2015) 3589–3590, https://doi.org/10.1073/pnas.1502590112.

[40] S. Deville, P. Berckmans, R. Van Hoof, I. Lambrichts, A. Salvati, I. Nelissen, Comparison of Extracellular Vesicle Isolation and Storage Methods Using High-Sensitivity Flow Cytometry, PLoS One 16 (2) (2021), e0245835, https://doi.org/10.1371/journal.pone.0245835.

[41] T.E. Whittaker, A. Nagelkerke, V. Nele, U. Kauscher, M.M. Stevens, Experimental artefacts can lead to misattribution of bioactivity from soluble mesenchymal stem cell paracrine factors to extracellular vesicles, J. Extracell. Vesicles 9 (1) (2020), https://doi.org/10.1080/20013078.2020.1807674.

[42] M. Cully, Exosome-based candidates move into the clinic, Nat. Rev. Drug Discov. 20 (1) (2021) 6–7, https://doi.org/10.1038/d41573-020-00220-y.

[43] H.H. Chang, C.J. Murphy, Mini Gold Nanorods with Tunable Plasmonic Peaks beyond 1000 Nm, Chem. Mater. 30 (4) (2018) 1427–1435, https://doi.org/10.1021/acs.chemmater.7b05310.

Plasmonic Gold Nanorods and β-Lapachone, ACS Appl. Bio Mater. 2 (2) (2019) 728–736, https://doi.org/10.1021/acsabm.8b00603.

[44] J.G. Mehtala, D.Y. Zemlyanov, J.P. Max, N. Kadasala, S. Zhao, A. Wei, Citrate-Stabilized Gold Nanorods, Langmuir 30 (46) (2014) 3727–13730, https://doi.org/10.1021/la5029542.

[45] C. Théry, S. Amigorena, G. Raposo, A. Clayton, Isolation and characterization of exosomes from cell culture supernatants and biological fluids, Curr. Protoc. cell Biol. 30 (1) (2006), https://doi.org/10.1002/0471143030.cb0322s30.

[46] J. Van Deun, P. Mestdagh, P. Agostinis, Ö. Akay, S. Anand, J. Anckaert, Z. A. Martinez, T. Baetens, E. Beghein, L. Bertier, G. Berx, J. Boere, S. Boukouris, M. Bremer, D. Buschmann, et al., EV-TRACK: transparent reporting and centralizing knowledge in extracellular vesicle research, Nat. Methods 14 (3) (2017) 228–232, https://doi.org/10.1038/nmeth.4185.

[47] T. Skotland, K. Sandvig, A. Llorente, Lipids in Exosomes: Current Knowledge and the Way Forward, Prog. Lipid Res. 66 (2017) 30–41, https://doi.org/10.1016/j.plipres.2017.03.001.

[48] J.G. Mehtala, A. Wei, Nanometric Resolution in the Hydrodynamic Size Analysis of Ligand-Stabilized Gold Nanorods, Langmuir 30 (46) (2014) 13737–13743, https://doi.org/10.1021/la502955h.

[49] R. Minnes, M. Nissinmann, Y. Maizels, G. Gerlitz, A. Katzir, Y. Raichlin, Using Attenuated Total Reflection-Fourier Transform Infra-Red (ATR-FTIR) Spectroscopy to Distinguish between Melanoma Cells with a Different Metastatic Potential, Sci. Rep. 7 (1) (2017) 1–7, https://doi.org/10.1038/s41598-017-04678-6.

[50] P. Zheng, Q. Luo, W. Wang, J. Li, T. Wang, P. Wang, L. Chen, P. Zhang, H. Chen, Y. Liu, P. Dong, G. Xie, Y. Ma, L. Jiang, X. Yuan, L. Shen, Tumor-Associated Macrophages-Derived Exosomes Promote the Migration of Gastric Cancer Cells by Transfer of Functional Apolipoprotein E, Cell Death Dis. 9 (4) (2018), https://doi.org/10.1038/s41419-018-0465-5.

[51] A. Llorente, T. Skotland, T. Sylvänne, D. Kauhanen, T. Róg, A. Orłowski, I. Vattulainen, K. Ekroos, K. Sandvig, Molecular Lipidomics of Exosomes Released by PC-3 Prostate Cancer Cells, Biochim. Biophys. Acta - Mol. Cell Biol. Lipids 1831 (7) (2013) 1302–1309, https://doi.org/10.1016/j.bbalip.2013.04.011.

[52] N. Singhto, A. Vinaiphat, V. Thongboonkerd, Discrimination of Urinary Exosomes from Microvesicles by Lipidomics Using Thin Layer Liquid Chromatography (TLC) Coupled with MALDI-TOF Mass Spectrometry, Sci. Rep. 9 (1) (2019) 1–11, https://doi.org/10.1038/s41598-019-50195-z.

[53] C. Théry, L. Zitvogel, S. Amigorena, Exosomes: Composition, Biogenesis and Function, Nat. Rev. Immunol. 2 (8) (2002) 569–579, https://doi.org/10.1038/nri855.

[54] M. Khongkow, T. Yata, S. Boonrungsiman, U.R. Ruktanonchai, D. Graham, K. Namdee, Surface Modification of Gold Nanoparticles with Neuron-Targeted Exosome for Enhanced Blood-Brain Barrier Penetration, Sci. Rep. 9 (1) (2019) 1–9, https://doi.org/10.1038/s41598-019-44569-6.

[55] M. Meister, R. Tikkanen, Endocytic Trafficking of Membrane-Bound Cargo: A Flotillin Point of View, Membranes (Basel). 4 (3) (2014) 356–371, https://doi.org/10.3390/membranes4030356.

[56] G. Merckx, B. Hosseinkhani, S. Kuypers, S. Deville, J. Irobi, I. Nelissen, L. Michiels, I. Lambrichts, A. Bronckaers, Angiogenic Effects of Human Dental Pulp and Bone Marrow-Derived Mesenchymal Stromal Cells and Their Extracellular Vesicles, Cells 9 (2) (2020) 312, https://doi.org/10.3390/cells9020312.

[57] J. Cancino-Bernardi, P.M.P. Lins, V.S. Marangoni, H.A.M. Faria, V. Zucolotto, Difference in Lipid Cell Composition and Shaped-Based Gold Nanoparticles Induce Distinguish Pathways in Langmuir Monolayers Response, Mater. Today Commun. 26 (2021), 101831, https://doi.org/10.1016/j.mtcomm.2020.101831.

[58] K. Knop, R. Hoogenboom, D. Fischer, U.S.S. Schubert, Poly(Ethylene Glycol) in Drug Delivery: Pros and Cons as Well as Potential Alternatives, Angew. Chemie Int. Ed. 49 (36) (2010) 6288–6308, https://doi.org/10.1002/anie.200902672.

[59] M. Moros, A. Lewinska, F. Merola, P. Ferraro, M. Wnuk, A. Tino, C. Tortiglione, Gold Nanorods and Nanoprisms Mediate Different Photothermal Cell Death Mechanisms in Vitro and in Vivo, ACS Appl. Mater. Interfaces 12 (12) (2020) 13718–13730, https://doi.org/10.1021/acsami.0c02022.

[60] P. Icard, L. Poulain, H. Lincet, Understanding the Central Role of Citrate in the Metabolism of Cancer Cells, Biochim. Biophys. Acta - Rev. Cancer 1825 (1) (2012) 111–116, https://doi.org/10.1016/j.bbcan.2011.10.007.

[61] V. Guerrero-Florez, S.C. Mendez-Sanchez, O.A. Patrón-Soberano, V. Rodríguez-González, D. Blach, O.F. Martínez, Gold nanoparticle-mediated generation of reactive oxygen species during plasmonic photothermal therapy: a comparative study for different particle sizes, shapes, and surface conjugations, J. Mater. Chem. B 8 (14) (2020) 2862–2875, https://doi.org/10.1039/D0TB00240B.

[62] B.S. Joshi, I.S. Zuhorn, Heparan Sulfate Proteoglycan-Mediated Dynamin-Dependent Transport of Neural Stem Cell Exosomes in an in Vitro Blood-Brain Barrier Model, Eur. J. Neurosci. 53 (3) (2020) 706–719, https://doi.org/10.1111/ejn.14974.

[63] C. Barrès, L. Blanc, P. Bette-Bobillo, S. André, R. Mamoun, H.J. Gabius, M. Vidal, Galectin-5 Is Bound onto the Surface of Rat Reticulocyte Exosomes and Modulates Vesicle Uptake by Macrophages, Blood 115 (3) (2010) 696–705, https://doi.org/10.1182/blood-2009-07-231449.

[64] H. Costa Verdera, J.J. Gitz-Francois, R.M. Schiffelers, P. Vader, Cellular Uptake of Extracellular Vesicles Is Mediated by Clathrin-Independent Endocytosis and Macropinocytosis, J. Control. Release 266 (2017) 100–108, https://doi.org/10.1016/j.jconrel.2017.09.019.

[65] S. Mayor, R.E. Pagano, Pathways of Clathrin-Independent Endocytosis, Nat. Rev. Mol. Cell Biol. 8 (8) (2007) 603–612, https://doi.org/10.1038/nrm2216.

[66] K.E. Mordue, B.R. Hawley, T.J. Satchwell, A.M. Toye, CD47 Surface Stability Is Sensitive to Actin Disruption Prior to Inclusion within the Band 3 Macrocomplex, Sci. Rep. 7 (1) (2017) 1–14, https://doi.org/10.1038/s41598-017-02356-1.

[67] R.A. Rebres, K. Kajihara, E.J. Brown, Novel CD47-Dependent Intercellular Adhesion Modulates Cell Migration, J. Cell. Physiol. 205 (2) (2005) 182–193, https://doi.org/10.1002/jcp.20379.

[68] A. Parodi, N. Quattrocchi, A.L. van de Ven, C. Chiappini, M. Evangelopoulos, J. O. Martinez, B.S. Brown, S.Z. Khaled, I.K. Yazdi, M.V. Enzo, L. Isenhart, M. Ferrari, E. Tasciotti, Synthetic Nanoparticles Functionalized with Biomimetic Leukocyte Membranes Possess Cell-like Functions, Nat. Nanotechnol. 8 (1) (2012) 61–68, https://doi.org/10.1038/nnano.2012.212.

[69] V. Mercier, M.H. Laporte, O. Destaing, B. Blot, C.M. Blouin, K. Pernet-Gallay, C. Chatellard, Y. Saoudi, C. Albiges-Rizo, C. Lamaze, S. Fraboulet, A. Petiot, R. Sadoul, ALG-2 Interacting Protein-X (Alix) Is Essential for Clathrin-Independent Endocytosis and Signaling, Sci. Rep. 6 (2016) 1–15, https://doi.org/10.1038/srep26986.

[70] A. Hoshino, B. Costa-Silva, T.-L. Shen, G. Rodrigues, A. Hashimoto, M. Tesic Mark, H. Molina, S. Kohsaka, A. Di Giannatale, S. Ceder, S. Singh, C. Williams, N. Soplop, K. Uryu, L. Pharmer, T. King, L. Bojmar, A.E. Davies, Y. Ararso, T. Zhang, H. Zhang, J. Hernandez, J.M. Weiss, V.D. Dumont-Cole, K. Kramer, L.H. Wexler, A. Narendran, G.K. Schwartz, J.H. Healey, K. Jørgen Labori, E. H. Kure, P.M. Grandgenett, M.A. Hollingsworth, M. de Sousa, S. Kaur, M. Jain, K. Mallya, S.K. Batra, W.R. Jarnagin, M.S. Brady, O. Fodstad, V. Muller, K. Pantel, A.J. Minn, M.J. Bissell, B.A. Garcia, Y. Kang, V.K. Rajasekhar, C.M. Ghajar, I. Matei, H. Peinado, J. Bromberg, D. Lyden, Tumour Exosome Integrins Determine Organotropic Metastasis, Nature 527 (7578) (2015) 329–335, https://doi.org/10.1038/nature15756.

[71] G. Fuhrmann, A. Serio, M. Mazo, R. Nair, M.M. Stevens, Active Loading into Extracellular Vesicles Significantly Improves the Cellular Uptake and Photodynamic Effect of Porphyrins, J. Control. Release 205 (2015) 35–44, https://doi.org/10.1016/j.jconrel.2014.11.029.

[72] X. Liu, Q. Jin, Y. Ji, J. Ji, Minimizing nonspecific phagocytic uptake of biocompatible gold nanoparticles with mixed charged Zwitterionic surface modification, J. Mater. Chem. 22 (5) (2012) 1916–1927, https://doi.org/10.1039/C1JM14178C.